Oil & Natural Gas Technology

DOE Award No.: DE-FC26-06NT42960

Quarterly Progress Report

Reporting Period: July-September 2007

Detection and Production of Methane Hydrate

Submitted by:
Rice University
University of Houston
George J. Hirasaki
Department of Chemical and Biomolecular Engineering
Rice University – MS 362
6100 Main St.
Houston, TX 77251-1892
Phone: 713-348-5416; FAX: 713-348-5478; Email: gjh@rice.edu

Prepared for:
United States Department of Energy
National Energy Technology Laboratory

December, 2007

Office of Fossil Energy

Table of Contents

Progress during Phase 2: July-September 2007

DOE Methane Hydrate Program Peer Review
Colorado School of Mines, Petroleum Hall, Golden Colorado
September 18-20, 2007

Presentations were made by Priyank Jaiswal, Brandon Dugan, Jerry Dickens, Kishore Mohanty, and George Hirasaki.

Task 5: Carbon Inputs and Outputs to Gas Hydrate Systems

5.1a Measure iodine in sediments
Date: 12/07
Status: 01/08 (one month shift because of change in disbursement of funds)

We have measured iodine concentrations in pore waters from several gas hydrate systems. We hope to complete the analyses this month and write up intitial results over the next month.

5.1b Constrain Corg inputs from iodine
Date: 10/08
Status: 10/08

We will measure the content and isotopic composition of organic carbon and carbonate in sediment from cores of several gas hydrate systems. We have collected most of the samples, although plan to visit the ODP repository (College Station) in late spring or early summer to collect additional samples.
Most analyses will be done this summer, although we anticipate examination of a small “trial batch” of samples from the Peru Margin in the next month.

5.2a Construct metal profiles in sediments
Date: 12/09
Status: 12/09*

We will measure metal contents in sediment from cores of several gas hydrate systems to constrain past hydrocarbon outputs via anaerobic oxidation of methane (AOM). Because initiation of project funding was slowed, we began some of this work last year with scientists from Japan using samples of opportunity from the Sea of Japan. This work was published in the fall (Snyder et al., 2007).

5.2b Modeling/integrating profiles
Date: 12/10
Status: 12/10

We will use the metal and iodine profiles to constrain models for gas hydrate formation. We have discussed data and models but have not begun this work so far.

Task 6: Numerical Models for Quantification of Hydrate and Free Gas Accumulations

Code development for simulation in 2-D has continued during the third quarter.

The sulfate-methane interface work was originally scheduled later in the project. However, since it only required analysis in 1-D, it was completed in the first year. Below is a short summary article that has been accepted by Geophysical Research Letters. A longer length article that includes the derivation of analytical solutions is being prepared.

The sulfate-methane transition as a proxy for average methane hydrate saturation in marine sediments

G. Bhatnagar[1], W. G. Chapman[1], G. R. Dickens[2], B. Dugan[2], G. J. Hirasaki[1*]

[1]*Department of Chemical & Biomolecular Engineering, Rice University, Houston, Texas*

[2]*Department of Earth Science, Rice University, Houston, Texas*

[*] *Corresponding author: gjh@rice.edu*

Abstract.

We develop a relationship between the sulfate-methane transition (SMT) and average gas hydrate saturation (AGHS) for systems dominated by methane migration from deeper sources. The relationship is explained by a one-dimensional numerical model that simulates gas hydrate accumulation in marine sediments. Higher methane fluxes result in shallow SMT depths and high AGHS, while lower methane fluxes result in deep SMTs and low AGHS. We also generalize the variation between AGHS and scaled SMT depth, a procedure that aids prediction of AGHS at different sites from observations of the SMT, such as along Cascadia Margin.

1. Introduction

Gas hydrates can form in the pore space of sediment along continental margins when methane and other low molecular weight gases combine with water at appropriate pressure, temperature and salinity conditions [*Kvenvolden*, 1993]. These hydrates are components of dynamic systems in which methane

enters and leaves a gas hydrate stability zone (GHSZ) at variable rates [*Dickens*, 2003]. Based on the supply of methane, marine gas hydrate systems can be distinguished into two end-members: *in-situ* systems where microbes generate methane within the GHSZ [e.g., *Claypool and Kvenvolden*, 1983]; and deep-source systems where rising fluids bring methane from depth [e.g., *Hyndman and Davis*, 1992]. However, quantifying gas hydrate saturation in these systems remains a challenge. In this paper, we develop a model that relates average gas hydrate saturation (AGHS) to the depth of sulfate-methane transition (SMT) in deep-source systems. This facilitates prediction of AGHS at sites where SMT depth is known.

The SMT denotes a relatively thin zone near the seafloor where pore water sulfate and methane are depleted to zero concentration (Figure 1). This depletion occurs due to the anaerobic oxidation of methane reaction (AOM: $CH_4 + SO_4^{2-} \rightarrow HCO_3^- + HS^- + H_2O$) [*Borowski et al.*, 1999]. Although microbes can also consume sulfate using solid organic carbon [*Berner*, 1980], AOM can dominate overall sulfate depletion in sediments with gas hydrates and modest methane fluxes [*Borowski et al.*, 1996; *Snyder et al.*, 2007]. Further, since we focus only on deep-source gas hydrate systems (i.e., sites with low organic carbon input), AOM becomes the only sulfate sink. The sulfate profile and SMT depth in such deep-source systems should depend on methane flux from below because of the simple 1:1 AOM reaction [*Borowski et al.*, 1996; *Snyder et al.*, 2007]. Additionally, the thickness of the gas hydrate zone and gas hydrate saturation are functions of upward methane flux [*Davie and Buffett*, 2003; *Bhatnagar et al.*, 2007]. Thus, SMT depth (L_s, Figure 1) should relate to gas hydrate saturation [*Borowski et al.*, 1999].

To study this relationship between SMT depth and AGHS, we expand the model of *Bhatnagar et al.* [2007] by including a sulfate balance for deep-source systems (Figure 1). We show that, at steady-state conditions, the depth of the SMT relates to net fluid flux in the system and to AGHS (volume fraction of pore space) within the GHSZ. Compared to previous site-specific studies, our model generalizes the relationship between SMT depth and AGHS at any gas hydrate setting dominated by methane flux from depth.

2. Mathematical Model for Gas Hydrate Accumulation and AOM

Gas hydrate accumulation in marine sediment is simulated using a numerical model that includes phase equilibrium, sedimentation, diffusion, compaction-driven fluid flow, and external fluid flow [*Bhatnagar et al.*, 2007]. Following *Bhatnagar et al.* [2007], the three-phase methane mass balance (liquid, gas hydrate and free gas) can be written to include the AOM reaction in dimensionless form as:

$$\frac{\partial}{\partial \tilde{t}}\left[\frac{1+\gamma\tilde{\phi}}{\gamma}\left(S_w\tilde{c}_m^w + S_h\tilde{c}_m^h\tilde{\rho}_h + S_g\tilde{c}_m^g\tilde{\rho}_g\right)\right] +$$

$$\frac{1+\gamma}{\gamma}\frac{\partial}{\partial \tilde{z}}\left[\begin{array}{l}\left(\left(Pe_1+Pe_2\right) - Pe_1\tilde{U}_s\frac{(1+\gamma\tilde{\phi})}{\gamma(1-\tilde{\phi})}S_h c_w^h\tilde{\rho}_h\right)\tilde{c}_m^w \\ +Pe_1\tilde{U}_s\frac{(1+\gamma\tilde{\phi})}{\gamma(1-\tilde{\phi})}\left(S_h\tilde{c}_m^h\tilde{\rho}_h + S_g\tilde{c}_m^g\tilde{\rho}_g\right)\end{array}\right] = \qquad (1)$$

$$\frac{\partial}{\partial \tilde{z}}\left[\frac{1+\gamma\tilde{\phi}}{\gamma}S_w\frac{\partial\tilde{c}_m^w}{\partial\tilde{z}}\right] - Da_{AOM}\frac{M_{CH_4}c_{s,0}^w}{M_{SO_4}c_{m,eqb}^w}\left[\frac{1+\gamma\tilde{\phi}}{\gamma}S_w\right]\tilde{c}_m^w\tilde{c}_s^w$$

where S_i represents saturation of phase i in pore space, $\tilde{\rho}_i$ is the density of phase i scaled by water density, M_j is molecular weight, and subscripts/superscripts w, h and g denote liquid water, hydrate and free gas phases, respectively. We normalize vertical depth as $\tilde{z} = z/L_t$, where L_t is depth to the base of GHSZ. Time is made dimensionless by a combination of L_t and methane diffusivity D_m ($\tilde{t} = t/(L_t^2/D_m)$).

Methane mass fraction in phase i (c_m^i) is scaled by methane solubility in the liquid phase at the base of GHSZ ($c_{m,eqb}^w$), c_w^h is mass fraction of water in hydrate phase ($c_w^h = 1 - c_m^h$), while sulfate mass fraction in pore water (c_s^w) is scaled by the seawater value ($c_{s,0}^w$), to get the corresponding normalized variables:

$$\tilde{c}_m^i = \frac{c_m^i}{c_{m,eqb}^w} \quad \text{for} \quad i \in \{w,h,g\} \quad , \qquad \tilde{c}_s^w = \frac{c_s^w}{c_{s,0}^w} \qquad (2)$$

Reduced porosity parameters, $\tilde{\phi}$ and γ, and normalized sediment flux, $\tilde{U}_s$, are defined as:

$$\tilde{\phi} = \frac{\phi - \phi_\infty}{1-\phi_\infty}, \qquad \gamma = \frac{1-\phi_\infty}{\phi_\infty}, \qquad \tilde{U}_s = \frac{U_s}{U_{f,sed}} \qquad (3)$$

where ϕ is sediment porosity, ϕ_∞ is the minimum porosity at great depth, U_s is sediment flux, and $U_{f,sed}$ is the fluid flux resulting from sedimentation and compaction. Porosity loss is related to depth using a constitutive relationship between porosity and vertical effective stress assuming hydrostatic pressure [*Bhatnagar et al.*, 2007]:

$$\tilde{\phi} = \frac{\eta}{\eta + (1-\eta)e^{\tilde{z}}}, \qquad \eta = \frac{\phi_0 - \phi_\infty}{1-\phi_\infty} \qquad (4)$$

where η and ϕ_0 are the reduced and actual porosities at the seafloor, respectively. $U_{f,sed}$ is related to seafloor sedimentation rate ($\dot{S}$) and porosities as follows [*Berner*, 1980]:

$$U_{f,sed} = \frac{1-\phi_0}{1-\phi_\infty}\dot{S}\phi_\infty \tag{5}$$

The two Peclet numbers Pe_1, Pe_2 and the Damkohler number Da_{AOM} are defined as:

$$Pe_1 = \frac{U_{f,sed}L_t}{D_m}, \qquad Pe_2 = \frac{U_{f,ext}L_t}{D_m}, \qquad Da_{AOM} = \frac{\rho_w c^w_{m,eqb}}{M_{CH_4}}\frac{\lambda_{AOM}L_t^2}{D_m} \tag{6}$$

where $U_{f,ext}$ is the upward fluid flux due to external sources and has negative value (due to opposite direction to $U_{f,sed}$), and λ_{AOM} is the second order rate constant for AOM. Thus, Pe_1 has positive value, while Pe_2 becomes negative. Since we focus on deep-source systems, results shown later are relevant for cases where $|Pe_2| > |Pe_1|$. Importantly, Pe_1 characterizes the ratio of compaction-driven fluid flux to methane diffusion, while Pe_2 represents the ratio of external fluid flux to methane diffusion. The Damkohler number compares AOM rate to methane diffusion. Finally, we complete the system by formulating the dimensionless sulfate mass balance:

$$\begin{aligned}&\frac{\partial}{\partial\tilde{t}}\left[\frac{1+\gamma\tilde{\phi}}{\gamma}S_w\tilde{c}_s^w\right]+\frac{1+\gamma}{\gamma}\frac{\partial}{\partial\tilde{z}}\left[\left(\left(Pe_1+Pe_2\right)-Pe_1\tilde{U}_s\frac{(1+\gamma\tilde{\phi})}{\gamma(1-\tilde{\phi})}S_h c_w^h\tilde{\rho}_h\right)\tilde{c}_s^w\right]=\\&\frac{\partial}{\partial\tilde{z}}\left[\frac{1+\gamma\tilde{\phi}}{\gamma}S_w\left(\frac{D_s}{D_m}\right)\frac{\partial\tilde{c}_s^w}{\partial\tilde{z}}\right]-Da_{AOM}\left[\frac{1+\gamma\tilde{\phi}}{\gamma}S_w\right]\tilde{c}_m^w\tilde{c}_s^w\end{aligned} \tag{7}$$

where D_s denotes sulfate diffusivity. The initial and boundary conditions for the two mass balances are written as:

I.C.: $\tilde{c}_s^w(\tilde{z},0) = \tilde{c}_m^w(\tilde{z},0) = 0$ (8)

B.C. (1): $\tilde{c}_s^w(0,\tilde{t}) = 1$, $\tilde{c}_m^w(0,\tilde{t}) = 0$ (9)

B.C. (2): $\frac{\partial\tilde{c}_s^w}{\partial\tilde{z}}(D,\tilde{t}) = 0$, $\tilde{c}_m^w(D,\tilde{t}) = \tilde{c}_{m,ext}^w = \frac{c_{m,ext}^w}{c_{m,eqb}^w}$ (10)

where $c_{m,ext}^w$ is the methane concentration in the external flux, $\tilde{c}_{m,ext}^w$ is the normalized value, and *D* denotes the bottom of the model domain.

3. Results

Equations (1) and (7) are solved numerically to obtain steady-state profiles for methane, gas hydrate saturation, and pore water sulfate concentration. For results shown later, we assume seafloor temperature (T_0) to be 3°C, geothermal gradient (G) to be 0.04°C/m, and pore water salinity representative of standard seawater. Changing T_0 or G results in methane solubility curves that are similar in the normalized form [*Bhatnagar et al.*, 2007], causing AGHS to be relatively insensitive to changes in T_0 or G. However, the normalized solubility curves are more sensitive to seafloor depth. Thus, we use a seafloor depth of 1000 m for results shown in Figures 2 and 3, whereas Figure 4 generalizes the relationship between AGHS and SMT depth for multiple seafloor depths. Porosity at the seafloor (ϕ_0) and at depth (ϕ_∞) are assumed to be 0.7 and 0.1, respectively. Diffusivities D_s and D_m are taken to be 0.56×10^{-9} and 0.87×10^{-9} m^2/s, respectively [*Iversen and Jørgensen*, 1993], c_m^h is set to 0.134, seawater sulfate concentration equals 28 mM, and ρ_h and ρ_f equal 930 and 1030 kg/m^3, respectively. At steady state, $\tilde{c}_{m,ext}^w$ is not significant, provided it exceeds the minimum required to form hydrate [*Bhatnagar et al.*, 2007]. Consequently, we assume in all simulations here that $\tilde{c}_{m,ext}^w$ equals unity.

We first study the effect of Da_{AOM} on steady-state profiles. For fixed Pe_1 and Pe_2, decreasing Da_{AOM} results in a thickening of the SMT zone (Figure 2a). Higher Da_{AOM} implies faster consumption of methane and sulfate compared to diffusion, causing a relatively sharp SMT. The thickness of the SMT zone is usually less than a few meters at most gas hydrate settings, so we use a large value of Da_{AOM} (10^8) in further simulations.

Concentration profiles simulated for three different sets of Pe_1 and Pe_2, but with the sum $Pe_1 + Pe_2$ held constant at -10, are shown in Figure 2b. Overlap of these profiles demonstrates that neither Pe_1 nor Pe_2 individually controls the concentration profiles, but that their sum determines the concentrations and the scaled SMT depth, $\tilde{L}_s = L_s / L_t$. This sum, $Pe_1 + Pe_2$, represents the net fluid flux through the system. Hydrate saturation profiles, however, depend on more than the sum of the Peclet numbers (Figure 2c). The AGHS ($\langle S_h \rangle$) for each of the three cases is about 0.2%, 0.5% and 2%, with the highest value corresponding to the smallest Pe_1 (0.1) and largest Pe_2 (-10.1). Small Pe_1 and large Pe_2 correspond to low sedimentation rate and high methane flux, respectively, resulting in higher AGHS. However, for all three cases, the product $Pe_1 \langle S_h \rangle$ is the same. Thus, Figure 2c demonstrates that $Pe_1 \langle S_h \rangle$, which characterizes the flux of gas hydrate through the GHSZ, is controlled by the net fluid flux, $Pe_1 + Pe_2$ [*Bhatnagar et al.*, 2007].

Increasing net methane flux from depth (i.e., raising the magnitude of $Pe_1 + Pe_2$) results in a shallow scaled SMT depth (Figure 3a), as proposed by *Borowski et al.* [1996, 1999]. Increasing Pe_2, with Pe_1 held constant, increases gas hydrate saturation (Figure 3b) due to higher methane input to the system. Consequently, $Pe_1 \langle S_h \rangle$ also increases. Hence, the scaled depth to the SMT, $\tilde{L}_s$, and $Pe_1 \langle S_h \rangle$ both depend on the sum $Pe_1 + Pe_2$. As a consequence, scaled SMT depth and $Pe_1 \langle S_h \rangle$ become correlated. This correlation, shown in Figure 4 for three seafloor depths, indicates that average gas hydrate flux, $Pe_1 \langle S_h \rangle$, increases as $\tilde{L}_s$ decreases. Thus, AGHS can be estimated for any system dominated by methane flux from depth if $\tilde{L}_s$ and Pe_1 are known (Figure 4).

4. Application to Cascadia Margin Sites

Sites drilled by Ocean Drilling Program (ODP) Leg 146 and Integrated Ocean Drilling Program Expedition (IODP) 311 penetrate gas hydrate accumulations along Cascadia Margin [*Westbrook et al.*, 1994; *Riedel et al.*, 2006]. The low organic carbon content of sediment and pervasive upward fluid migration at these sites suggests that gas hydrate in the Cascadia Margin is controlled by methane supplied from depth [*Riedel et al.*, 2006]. We now summarize calculation of AGHS from site-specific data at Cascadia Margin Sites 889, U1325, U1326 and U1328 (Table 1):

- Use sedimentation rate ($\dot{S}$) to calculate Pe_1 from equations (5) and (6);
- Calculate the scaled SMT depth $\tilde{L}_s$ using the dimensional depths L_s and L_t;
- For given seafloor depth and $\tilde{L}_s$, obtain gas hydrate flux $Pe_1 \langle S_h \rangle$ from Figure 4;
- Divide this gas hydrate flux by Pe_1 to yield AGHS, $\langle S_h \rangle$ (Table 1)

At Site 889 (ODP Leg 146), pore water chloride profile indicates a peak hydrate saturation close to 2% at the base of GHSZ, and AGHS <1% within the GHSZ [*Davie and Buffett*, 2003]. This result agrees favorably with our simulation that shows peak saturation of about 2.2 % at the base of GHSZ and AGHS of 0.4% across the entire GHSZ (Table 1). *Hyndman et al.* [1999] calculated gas hydrate saturation between 25-30% of pore space in the 100 m interval above the base of GHSZ at Site 889 using resistivity log data. Subsequent calculations using a different set of Archie parameters revise this estimate to 5-10% in that 100 m interval [*Riedel at al.,* 2006]. Further, *Ussler and Paull* [2001] show that a smoothly decreasing chlorinity profile at Site 889 yields hydrate saturation of 2-5% within discrete layers. Although several parameter uncertainties confront

such estimates [*Egeberg and Dickens*, 1999; *Riedel et al*., 2006], AGHS predicted using our SMT model concurs with the lower estimates at Site 889.

For the IODP Expedition 311 sites, drilled along the northern Cascadia Margin, we compare our predictions with AGHS computed from chloride anomalies and resistivity log data (Table 1). AGHS is calculated from chloride data by assuming a background *in situ* chloride profile and attributing the relative pore water freshening to gas hydrate dissociation [e.g., *Egeberg and Dickens*, 1999]. AGHS is obtained from resistivity data using the Archie equation and parameters given in *Riedel et al.* [2006]. AGHS at Sites U1325 and U1326 estimated from resistivity and chlorinity are similar and our predictions based on SMT depth are close to these estimates (Table 1). At Site U1328, our predicted AGHS is distinctly lower than resistivity-based estimate (Table 1). Site U1328 is a cold vent characterized by focused fluid and gas flow that causes high gas hydrate saturations close to the seafloor [*Riedel et al*., 2006]. Such local heterogeneities that might enhance methane flux from depth are not included in our simple 1-D model, thereby causing greater deviation between predicted and estimated AGHS.

Overall, we get good first order agreement between AGHS derived from chloride anomalies/resistivity logs and those predicted using our model, although our simulations consistently show lower AGHS at these sites. A possible explanation for this general deviation is that interpretations of resistivity logs depend on knowledge of formation water resistivity and three empirical constants, which are hard to constrain in clay-rich sediments. Additionally, our simulations (Figures 2 and 3) and previous models [e.g., *Davie and Buffett*, 2003] predict gas hydrate to first occur well below the seafloor. In contrast, log-based results often predict hydrate starting immediately below the seafloor, causing AGHS to be higher than that predicted from simple transport models. Apart from the small deviations between model and chloride/resistivity log predictions, our model captures the trend in the lateral variation of AGHS correctly and likely provides a lower bound on AGHS. Hence, our model and generalized results (Figure 4) provide a simple and fast technique to constrain AGHS in deep-source gas hydrate systems.

5. Conclusions

We show that scaled depth to the SMT ($\tilde{L}_s$) can be used to estimate AGHS for deep-source gas hydrate systems. Simulation results demonstrate that the net fluid flux controls $\tilde{L}_s$ and the average gas hydrate flux ($Pe_1 \langle S_h \rangle$) through the GHSZ, thereby allowing us to correlate $\tilde{L}_s$ and $Pe_1 \langle S_h \rangle$. Results also show that conditions that create shallow $\tilde{L}_s$ and low Peclet number (Pe_1) lead to higher AGHS. Application of this method to sites along Cascadia Margin reveals a good match with saturations estimated from chloride/resistivity log data and accurately predicts the lateral variability in AGHS.

Acknowledgments. We acknowledge financial support from the Shell Center for Sustainability, the Kobayashi Graduate Fellowship, and the Department of Energy (DE-FC26-06NT42960). We thank Janice Hewitt for help with editing this manuscript. Comments from anonymous reviewers improved this manuscript.

References

Berner, R. A. (1980), *Early Diagenesis : A Theoretical Approach*, Princeton Univ. Press, Princeton, N.J.

Bhatnagar, G., W. G. Chapman, G. R. Dickens, B. Dugan, and G. J. Hirasaki (2007), Generalization of gas hydrate distribution and saturation in marine sediments by scaling of thermodynamic and transport processes, *Am. J. Sci.*, *307*, 861-900.

Borowski, W. S., C. K. Paull, and W. Ussler III (1996), Marine pore-water sulfate profiles indicate in situ methane flux from underlying gas hydrate, *Geology*, *24(7)*, 655-658.

Borowski, W. S., C. K. Paull, and W. Ussler III (1999), Global and local variations of interstitial sulfate gradients in deep-water, continental margin sediments: Sensitivity to underlying methane and gas hydrates, *Mar. Geol.*, *159*, 131-154.

Claypool, G. E., and K. A. Kvenvolden (1983), Methane and other hydrocarbon gases in marine sediment, *Annu. Rev. Earth Planet. Sci.*, *11*, 299-327.

Davie, M. K., and B. A. Buffett (2003), Sources of methane for marine gas hydrate: inferences from a comparison of observations and numerical models, *Earth Planet. Sci. Lett.*, *206*, 51-63.

Dickens, G. R. (2003), Rethinking the global carbon cycle with a large, dynamic and microbially mediated gas hydrate capacitor, *Earth Planet. Sci. Lett.*, *213*, 169-183.

Hyndman, R. D., and E. E. Davis (1992), A mechanism for the formation of methane hydrate and seafoor bottom-simulating reflectors by vertical fluid expulsion, *J. Geophys. Res. B*, *97*, 7025-7041.

Hyndman, R. D., T. Yuan, and K. Moran (1999), The concentration of deep sea gas hydrates from downhole electrical resistivity logs and laboratory data, *Earth Planet. Sci. Lett.*, *172*, 167-177.

Iversen, N., and B. B. Jørgensen (1993), Diffusion coefficients of sulfate and methane in marine sediments: Influence of porosity, *Geochim. Cosmochim. Acta*, *57*, 571-578.

Kvenvolden, K. A. (1993), Gas hydrates: Geological perspective and global change, *Rev. Geophys.*, *31*, 173-187.

Riedel, M., T. S. Collett, M. J. Malone, and the Expedition 311 Scientists (Eds.) (2006), *Proc. IODP*, vol. 311, Integrated Ocean Drilling Program Management International Inc., Washington, DC.

Snyder, G. T., A. Hiruta, R. Matsumoto, G. R. Dickens, H. Tomaru, R. Takeuchi, J. Komatsubara, Y. Ishida, and H. Yu (2007), Pore water profiles and authigenic mineralization in shallow marine sediments above the methane-charged system on Umitaka Spur, Japan Sea, *Deep-Sea Res. II*, *54*, 1216-1239.

Ussler, W., and C. K. Paull (2001), Ion exclusion associated with marine gas hydrate deposits, in *Natural Gas Hydrates: Occurrence, Distribution, and Detection*, *Geophys. Monogr. Ser.*, vol. 124, edited by C. K. Paull and W. P. Dillon, pp. 41{51, AGU, Washington, D. C.

Westbrook, G. K., B. Carson, and R. J. Musgrave et al. (Eds.) (1994), *Proc. ODP, Initial Reports*, vol. 146 (Pt. 1), Ocean Drilling Program, College Statiom, TX.

Table 1. Site-specific parameters and calculated AGHS for Cascadia Margin sites compared with estimates from resistivity log data and chloride anomalies

Site	$\dot{S}$ (cm/k.y.)	Pe_1	Seafloor depth (m)	L_s / L_t (m/m) = $\tilde{L}_s$	$Pe_1 \langle S_h \rangle$ (Figure 4)	$\langle S_h \rangle$ (calc.)	$\langle S_h \rangle$ (res. log)	$\langle S_h \rangle$ (Cl^-)
889[a]	25	0.07	1311	10/225 = 0.044	0.03	0.4%	-	<1% [b]
U1325[c]	38.3	0.11	2195	4.5/230 = 0.02	0.22	2%	3.7%[e]	5.3%[f]
U1326[c]	38.3[g]	0.11	1828	2.5/230 = 0.011	0.46	4.2%	6.7%[e]	5.5%[f]
U1328[c]	34.3	0.09	1267	1.5/219 = 0.007	0.67	7.4%	12.6%[e]	-

[a] ODP Leg 146 [*Westbrook et al.*, 1994]

[b] Taken from numerical model of *Davie and Buffett*, 2003

[c] IODP Expedition 311 [*Riedel et al.*, 2006]

[e] Calculated from Archie equation using resistivity log data [*Riedel et al.*, 2006]

[f] Calculated using relative freshening of pore water chloride profiles [*Riedel et al.*, 2006]

[g] $\dot{S}$ was not available, hence assumed equal to rate at nearest site U1325

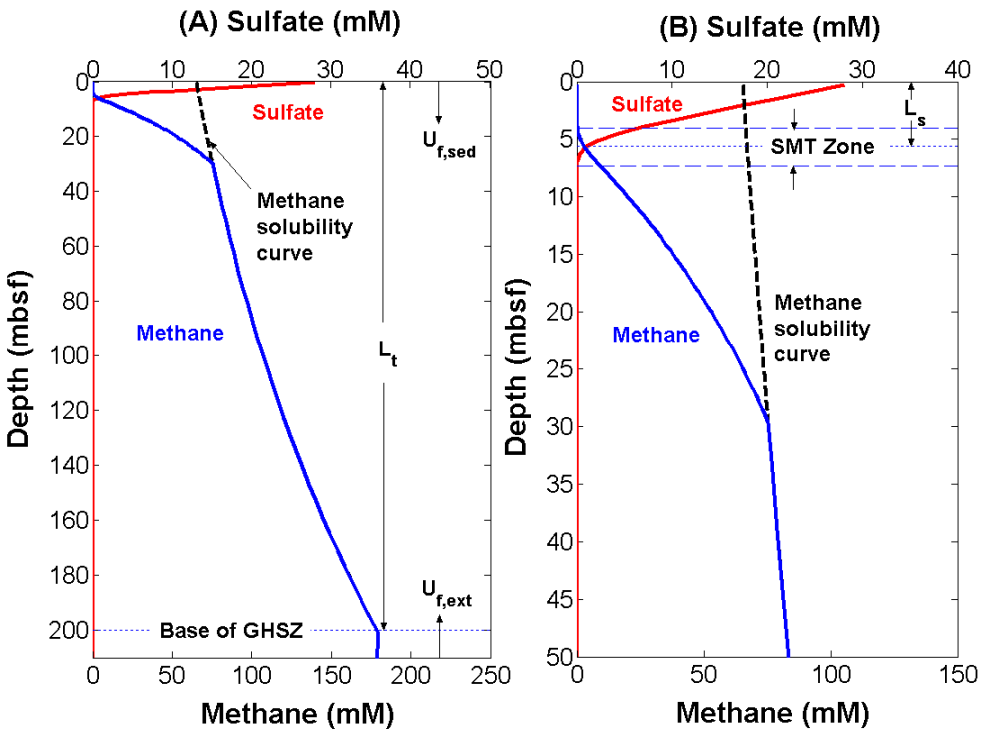

Figure 1. (A) Schematic representation of a gas hydrate system showing pore water sulfate and methane concentrations, which go to zero at some shallow depth because of anaerobic oxidation of methane (AOM). Also shown are methane solubility in water, the two fluid fluxes ($U_{f,sed}$ and $U_{f,ext}$), and depth to the base of the gas hydrate stability zone (L_t). (B) Close-up of the sulfate-methane transition (SMT) showing overlap of sulfate and methane profiles, and its depth below the seafloor (L_s).

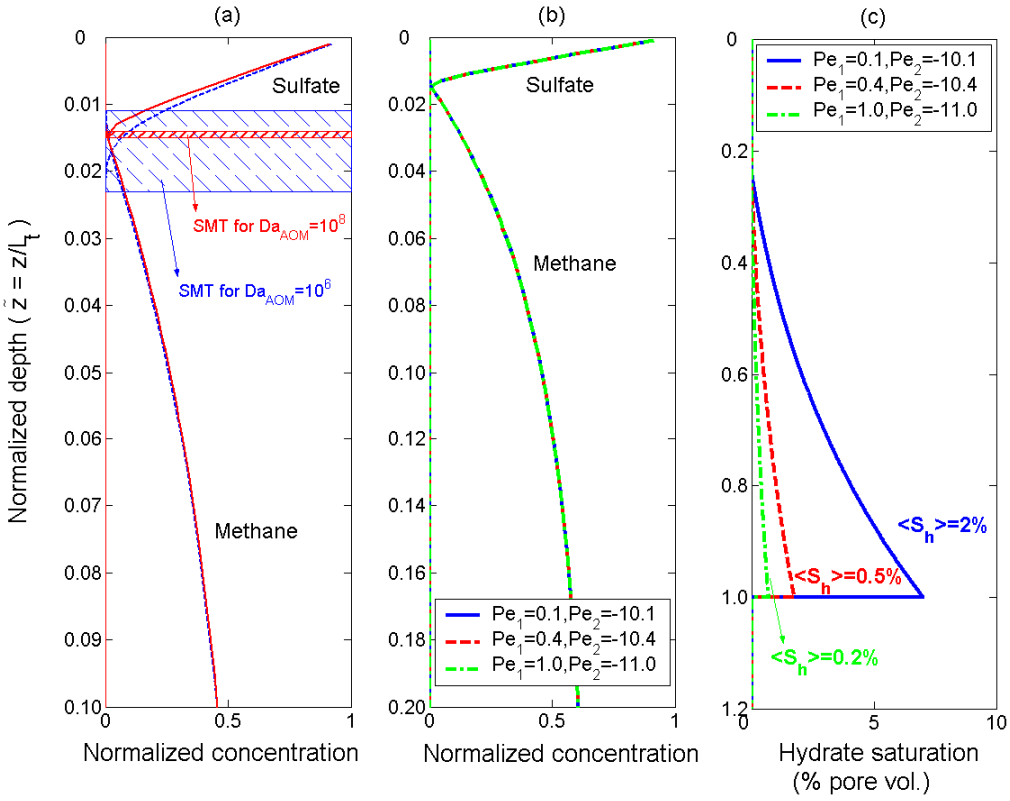

Figure 2. Effect of Damkohler number (Da_{AOM}) and Peclet numbers (Pe_1 , Pe_2) on steady-state profiles. $Pe_1 + Pe_2 = -10$ for all cases. Note different y-axis scale for each plot. (a) Sulfate and methane profiles for Da_{AOM} = 10^8 (solid curves) and Da_{AOM} = 10^6 (dashed curves). Hatched regions compare the thickness of the SMT for the two cases. (b) Simulations for different sets of Pe_1 and Pe_2, with $Pe_1 + Pe_2 = -10$. Overlap of methane and sulfate profiles shows that $Pe_1 + Pe_2$ controls the concentrations. (c) The product $Pe_1 \langle S_h \rangle$ depends on $Pe_1 + Pe_2$, but hydrate saturation profiles are a function of Pe_1.

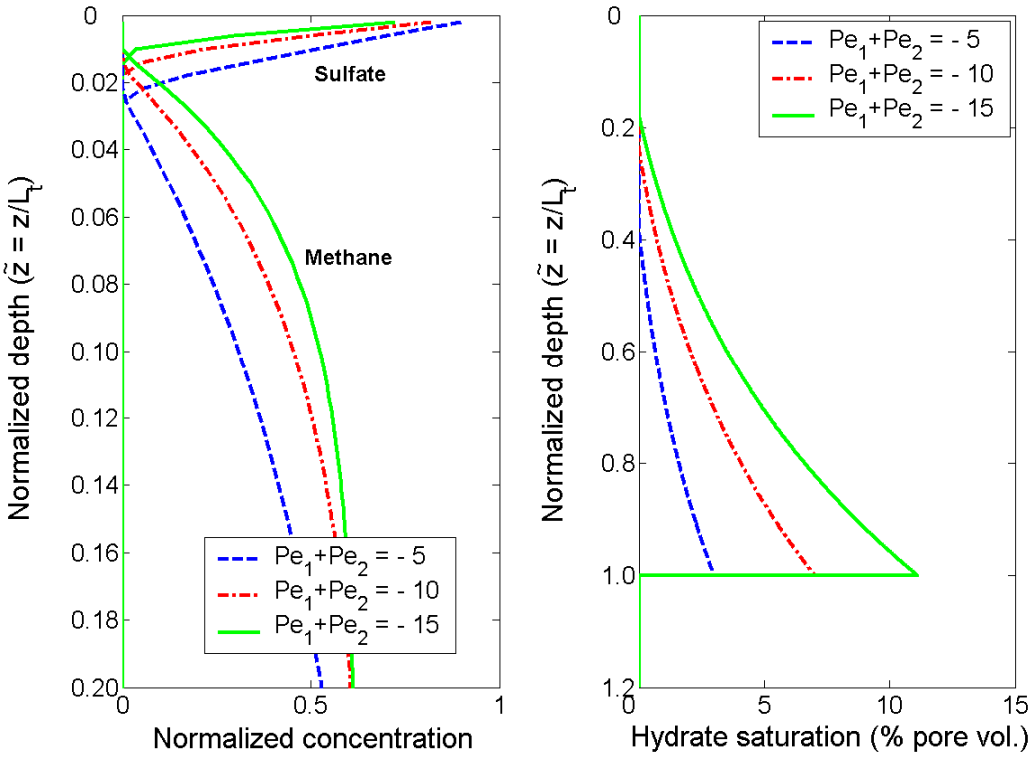

Figure 3. Effect of net fluid flux ($Pe_1 + Pe_2$) on steady-state concentrations. Pe_1 equals 0.1 for all simulations. (a) High magnitude of $Pe_1 + Pe_2$ defines higher net methane fluxes, resulting in shallower SMT zones. (b) Gas hydrate saturation at steady state increases as magnitude of $Pe_1 + Pe_2$ increases.

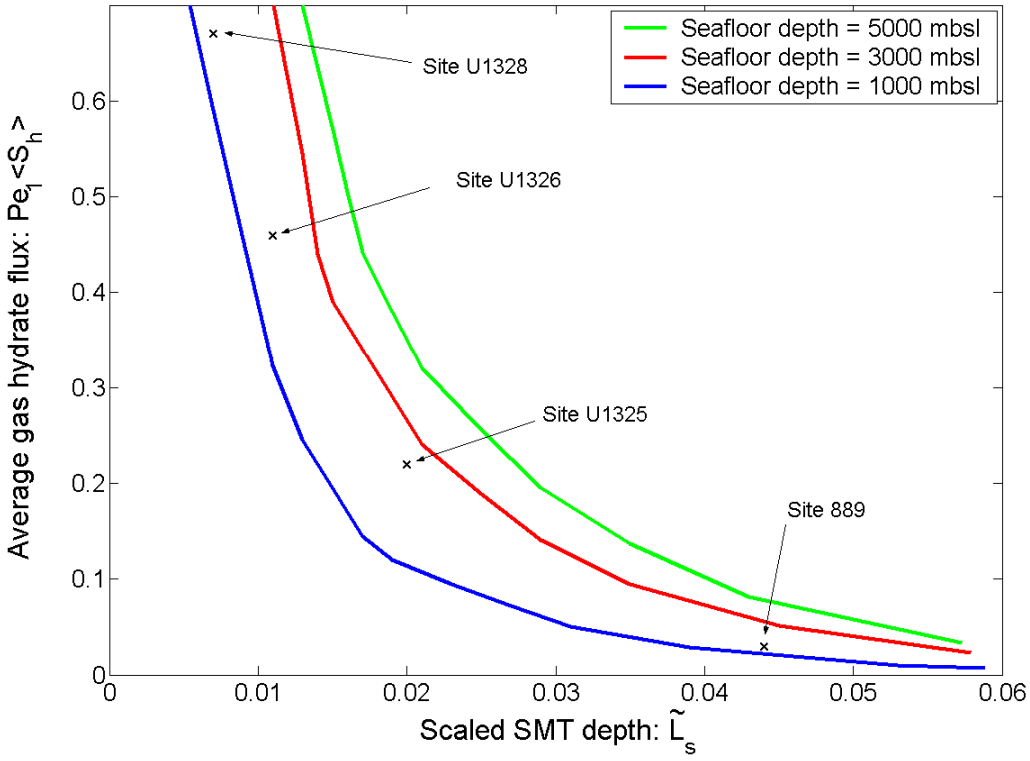

Figure 4. Relationship between average gas hydrate flux $Pe_1\langle S_h\rangle$ and scaled SMT depth ($\tilde{L}_s = L_s / L_t$) for several seafloor depths. Points corresponding to four Cascadia Margin sites are plotted to show how AGHS is estimated from $\tilde{L}_s$ using this plot (Table 1).

Task 7: Analysis of Production Strategy

J. Phirani & K. K. Mohanty, University of Houston

Abstract

In subtask 7.1, we are participating in the NETL methane code comparison study. In the last few months, we have worked on the first four problems set up by the Code Comparison Study group. The results for the first two problems were given in the first quarterly report. The brief statement of the second and third problems are described below along with our simulator results. Our results for the first four problems have been communicated to Prof. Brian Anderson, the coordinator of the Code Comparison Study group.

Problem 3.1

This is a problem of gas production inside a one-dimensional porous medium using thermal stimulation at one boundary keeping the pressure constant and no mass / heat flow at the other boundary. The initial pressure and temperature are specified for a hydrate saturation of 0.5 and aqueous saturation of 0.5. The domain is of length 1.5 meters, divided in 30 grid blocks of equal dimension. The parameters were recorded at the end of 1hr, 3hrs, 6hrs, 12 hrs, 1 day, 2 days, 3 days, 5 days.

The results from our simulator are plotted in Figs. 1-4. Fig. 1 shows the temperature evolution. Thermal stimulation is given at x=0 boundary; temperature increases with time, starting at x=0. At the point where the hydrate dissociation takes place, temperature remains at the triple point of hydrate, aqueous and gas phase. Fig. 2 shows the gas phase pressure. It shows a small increase in magnitude at the region where hydrate dissociation takes place and gas is produced. Fig. 3 shows the hydrate phase saturation. The hydrate saturation is low at the left section of the medium, but shows an increase on the right side of the dissociation region. The gas pressure is the highest at the dissociation region and decreases in both directions. On the right side of the dissociation region, gas combines with the already existing water to form hydrates because the pressure increases locally and temperature is still low. Fig. 4 shows the aqueous saturation which shows a dip in the saturation on the right side of the dissociation region.

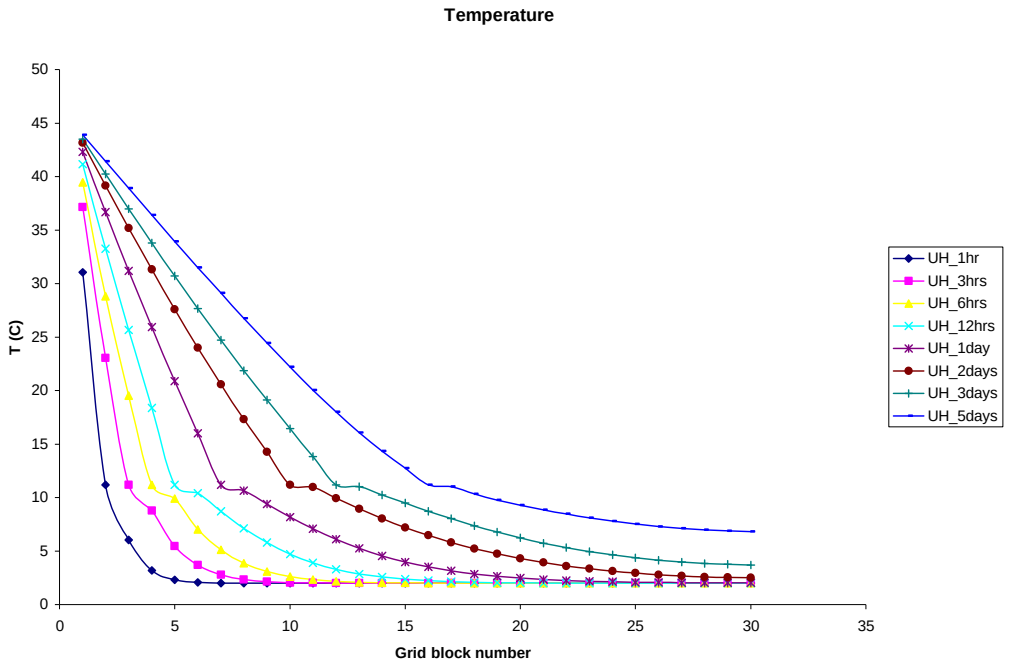

Fig. 1: Temperature evolution in problem 3.1

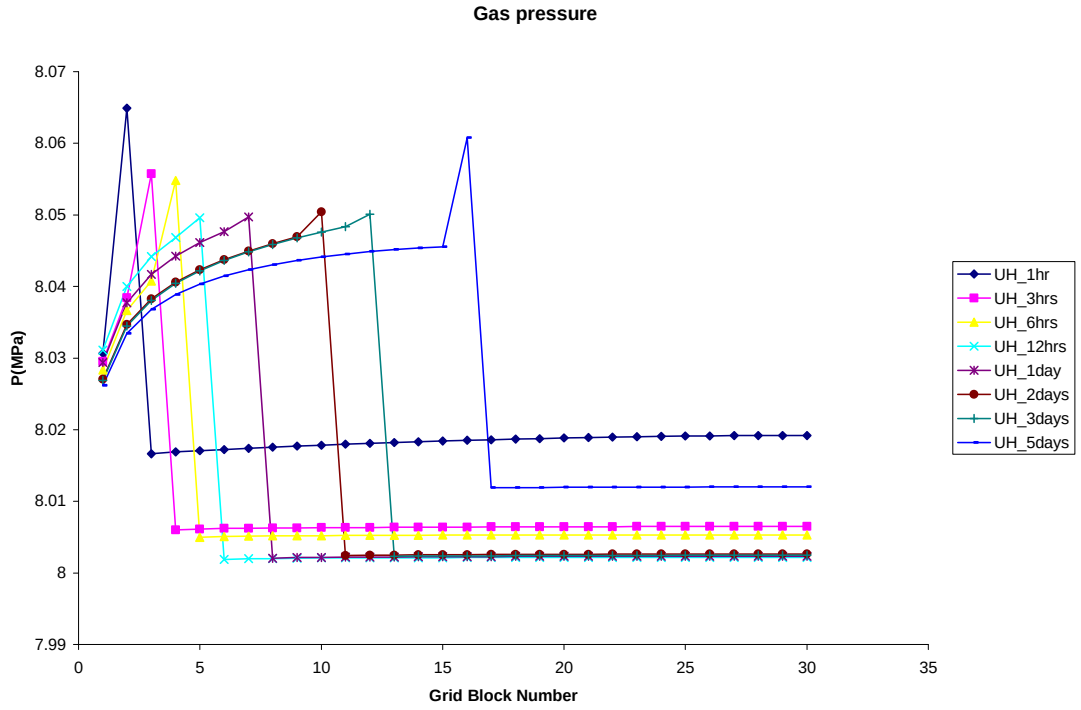

Fig. 2: Gas pressure evolution in problem 3.1

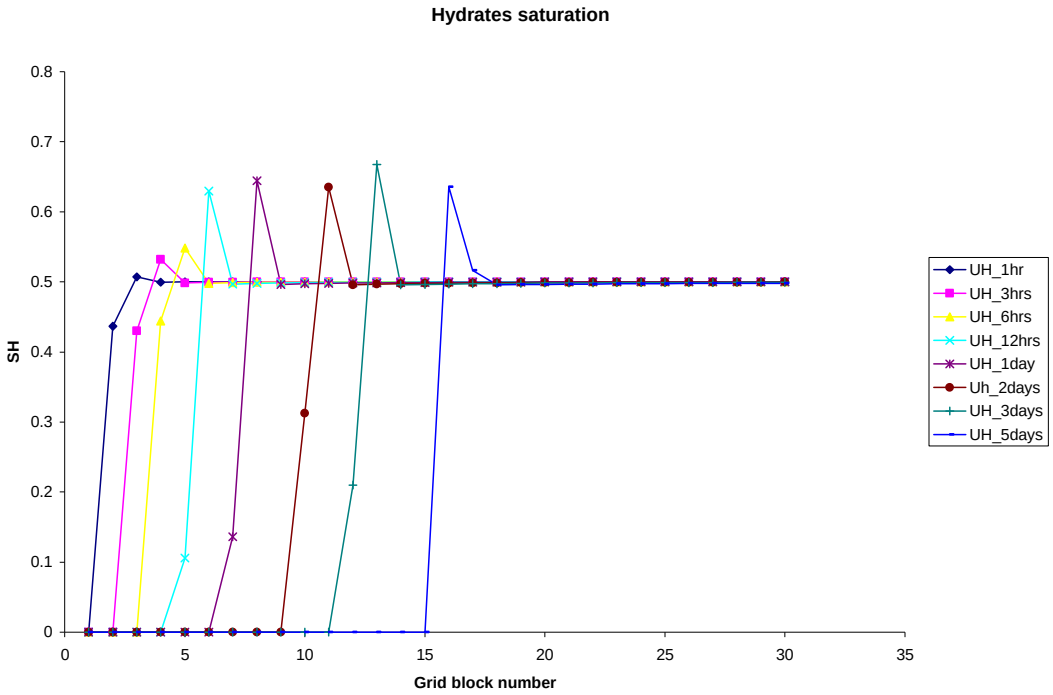

Fig. 3: Hydrate saturation evolution in problem 3.1

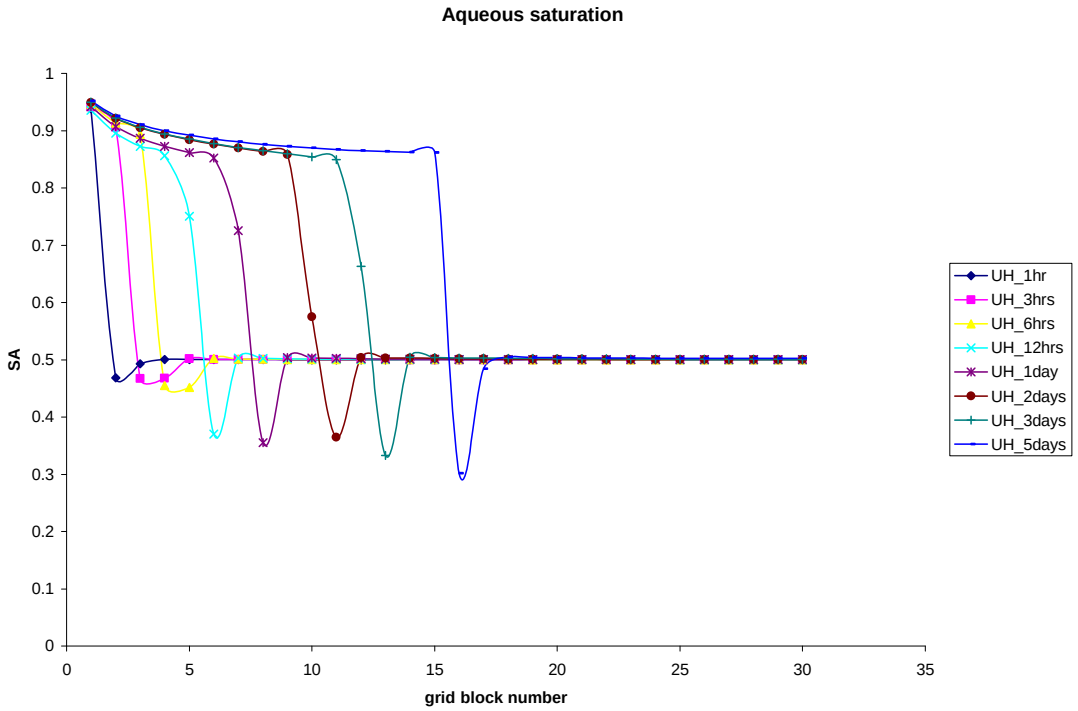

Fig. 4: Aqueous saturation evolution in problem 1

Problem 3.2

This is a one-dimensional gas production problem using depressurization, instead of thermal stimulation. The pressure decrease is enough for hydrates to dissociate, but small enough not form ice. The domain and the initial conditions are the same as in problem 3.1 and with no flow / heat transfer boundary conditions at x = Xmax and constant pressure of 2.8 MPa boundary condition at x=0. The initial hydrate and aqueous saturations are 0.5. The results are recorded at 2 min, 5 min, 20 min, 1 hr, 1.5 hr, 12 hr, 1 day, 2 day and 3 day.

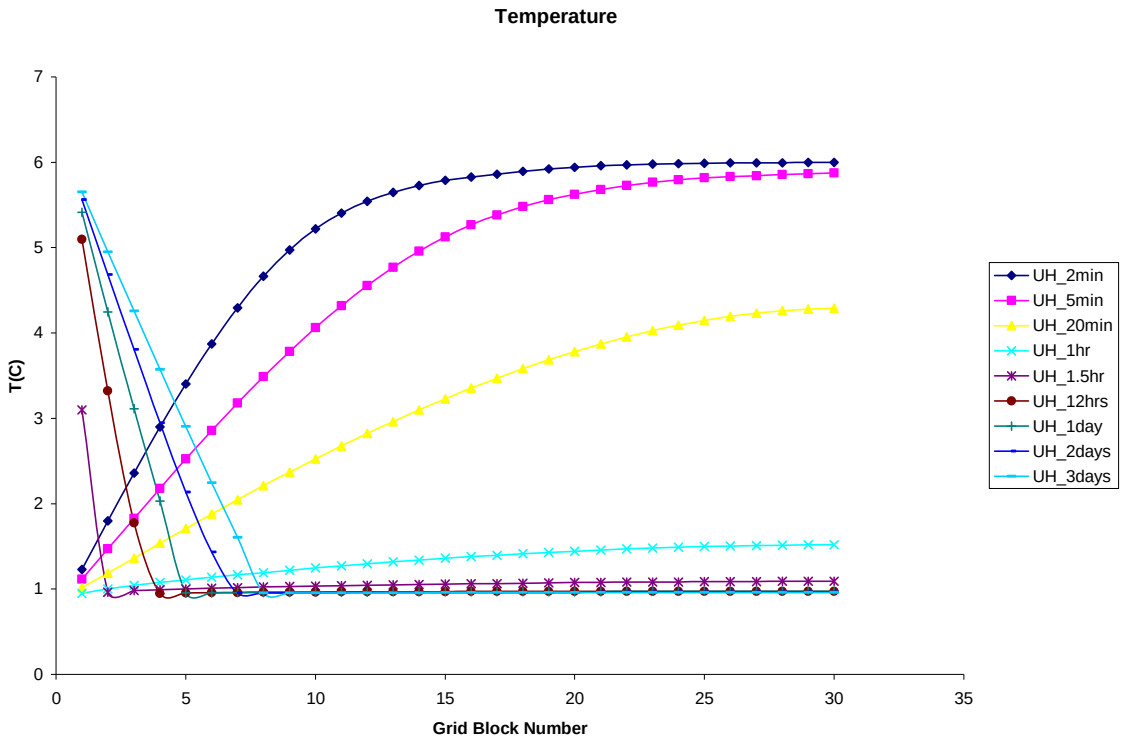

Fig. 5: Temperature evolution in problem 3.2

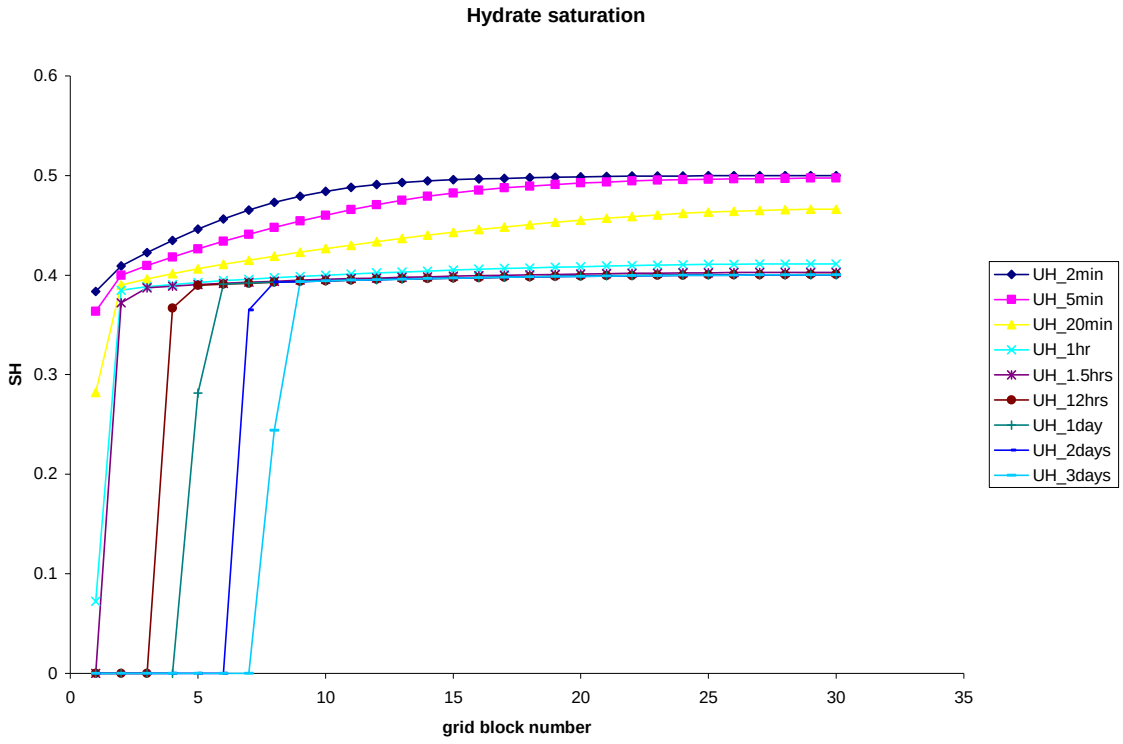

Fig. 6: Hydrate saturation evolution in problem 3.2

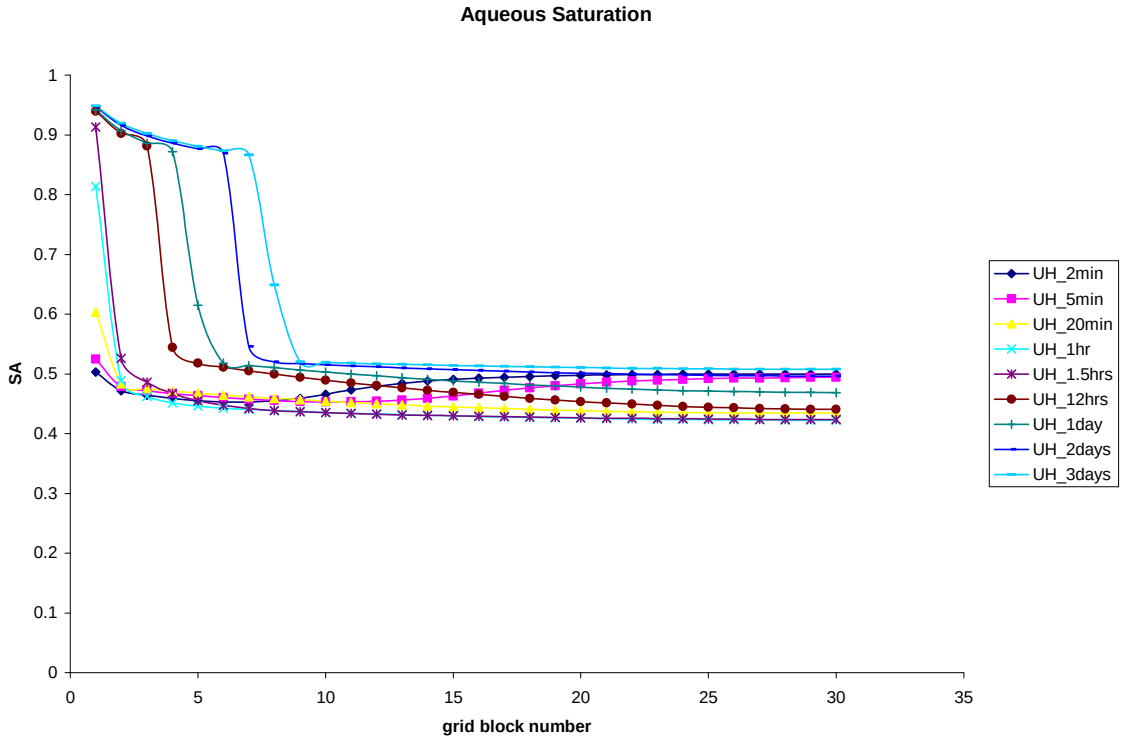

Fig. 7: Aqueous saturation evolution in problem 3.2

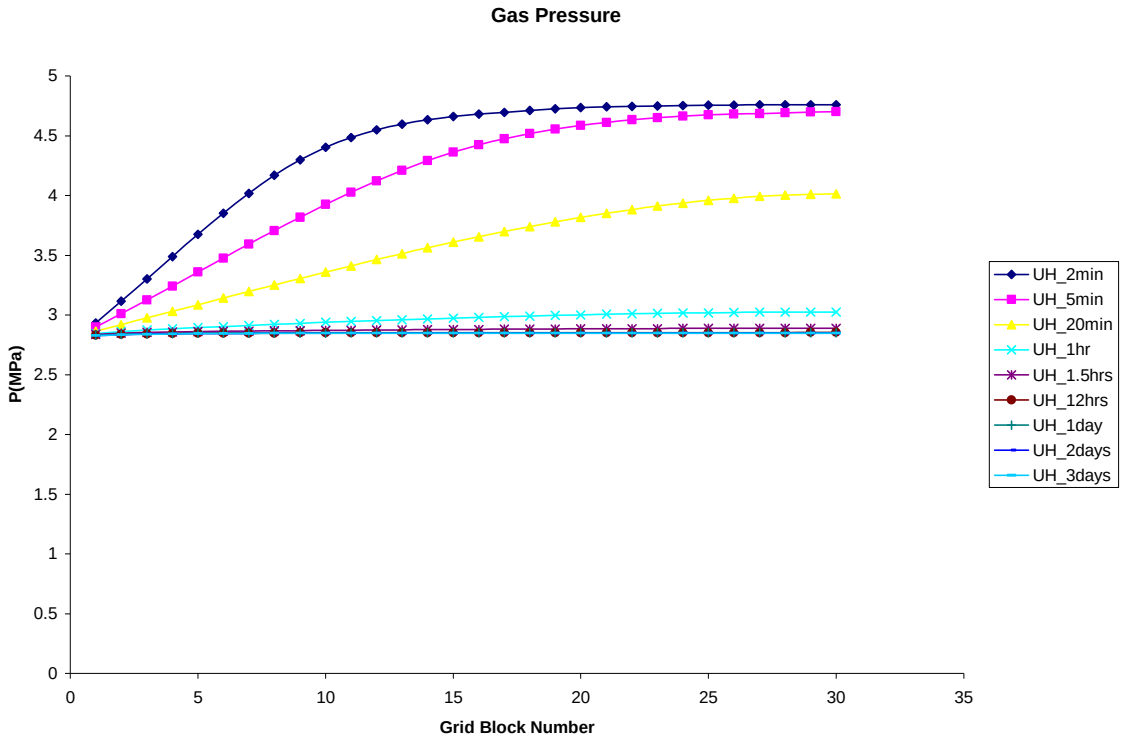

Fig. 8: Gas pressure evolution in problem 3.2

The results from our simulator for the problem 3.2 are plotted in Figs. 5-8. Fig. 5 shows the temperature evolution. There is an initial temperature decrease because the latent heat of dissociation is consumed for hydrate dissociation. The temperature at x=0 is kept constant at T=6 °C so the heat flux from x=0 increases the temperature at initial grid blocks as the dissociation front moves away from the boundary. Fig. 6 shows the hydrate phase saturation. As aqueous saturation is high through out the domain, pressure is conveyed very fast (shown in Fig 8) to the end of domain. Thus, the hydrate saturation decreases throughout the domain. There is also a larger dissociation front which propagates from the left boundary and dissociates all the hydrates. Fig. 7 shows the aqueous saturation evolution.

Problem 3.3

This is a one-dimensional gas production problem using depressurization like the last problem, but the applied boundary pressure is so low that temperature goes below freezing inside the domain. The domain is the same as in problem 3.2 and with no flow or heat transfer boundary conditions at x= Xmax and constant pressure of 0.5 MPa boundary condition at x=0. The problem is initialized with hydrate and aqueous phases at 0.5 saturation. The parameters are recorded at 2 min, 5 min, 10 min, 20 min, 30 min, 45 min, 1 hr, 1day and 5 day.

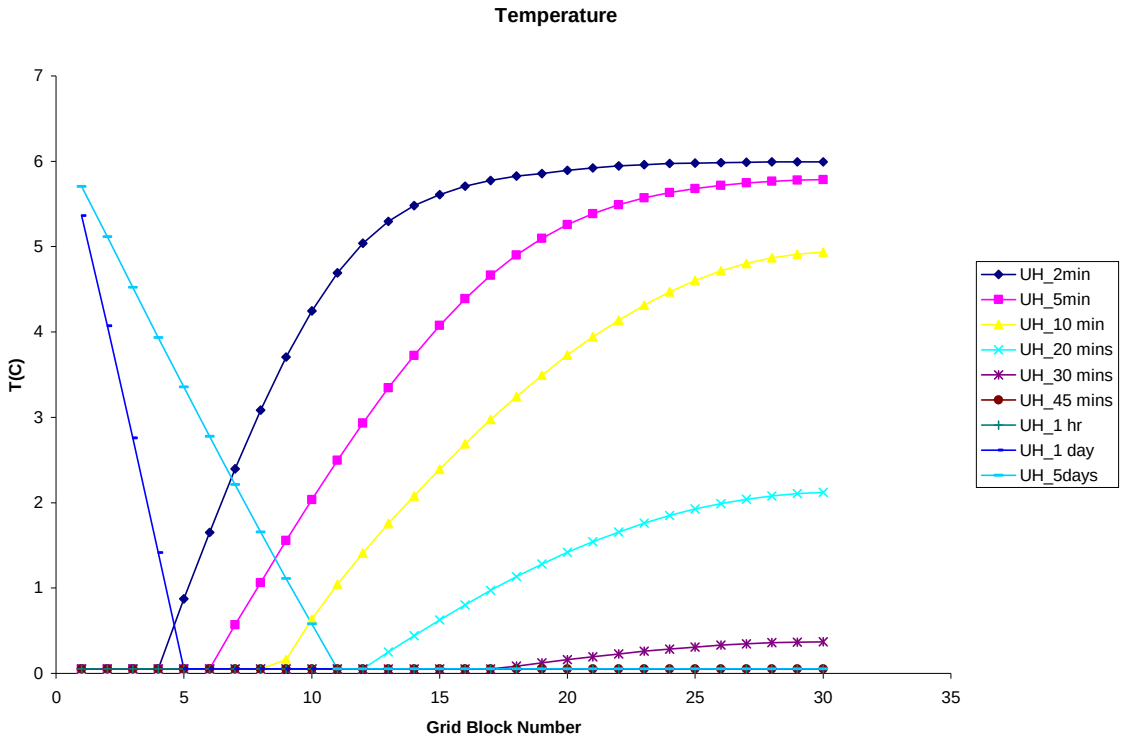

Fig. 9: Temperature evolution in problem 3.3

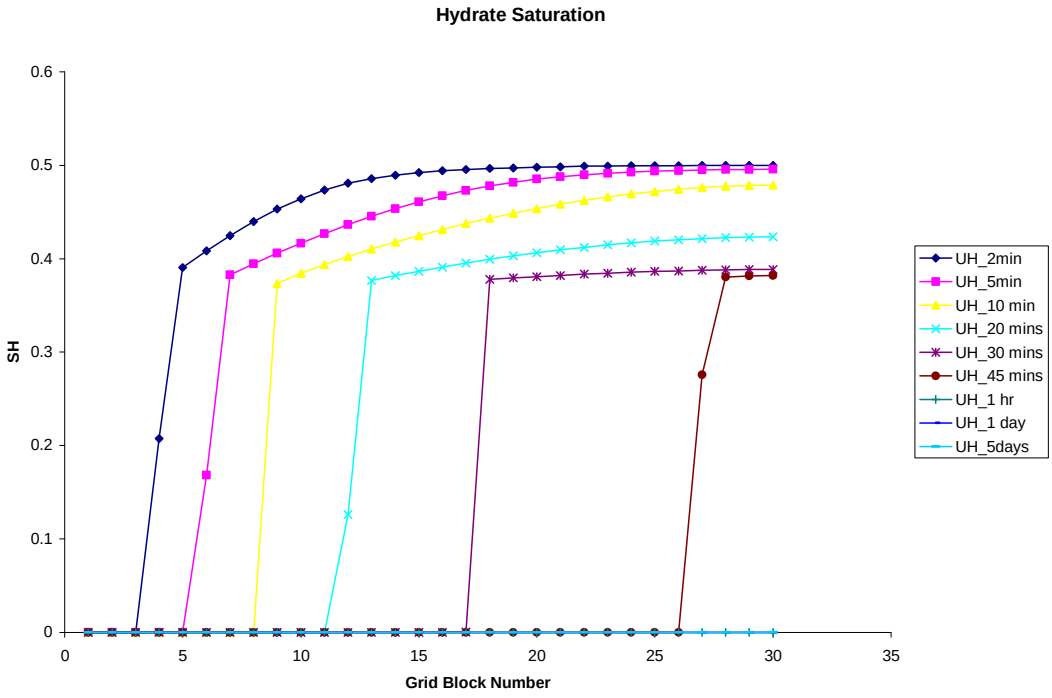

Fig. 10: Hydrate saturation evolution in problem 3.3

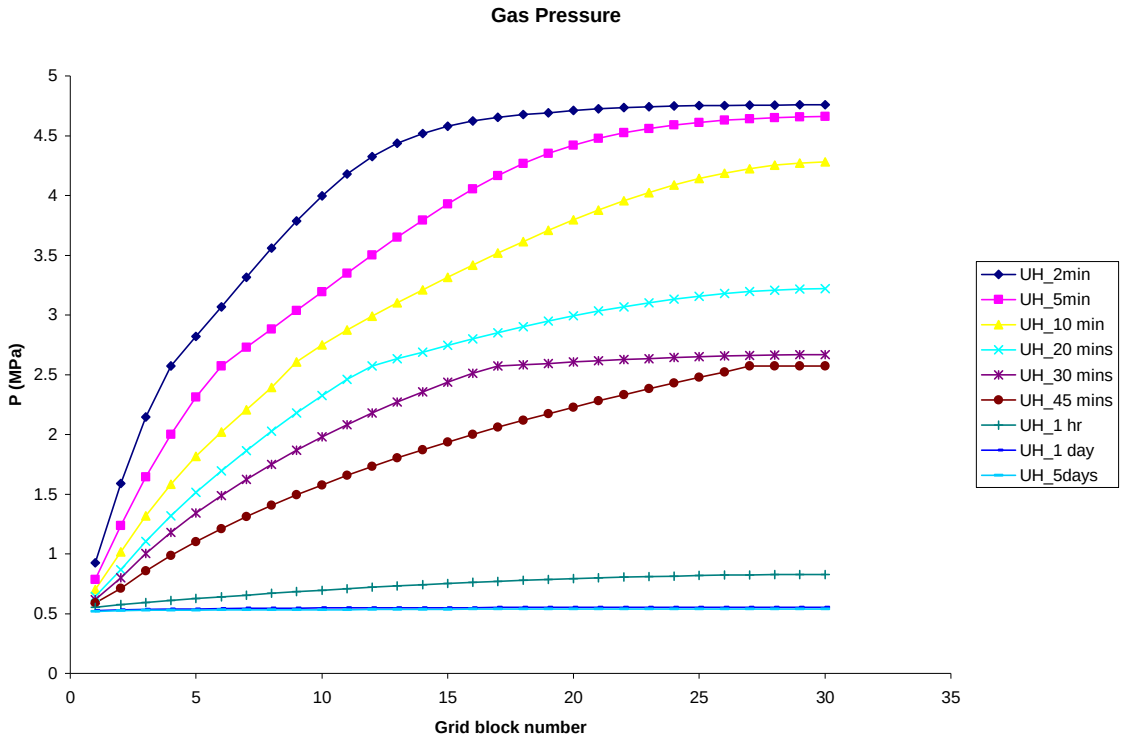

Fig. 11: Gas pressure evolution in problem 3.3

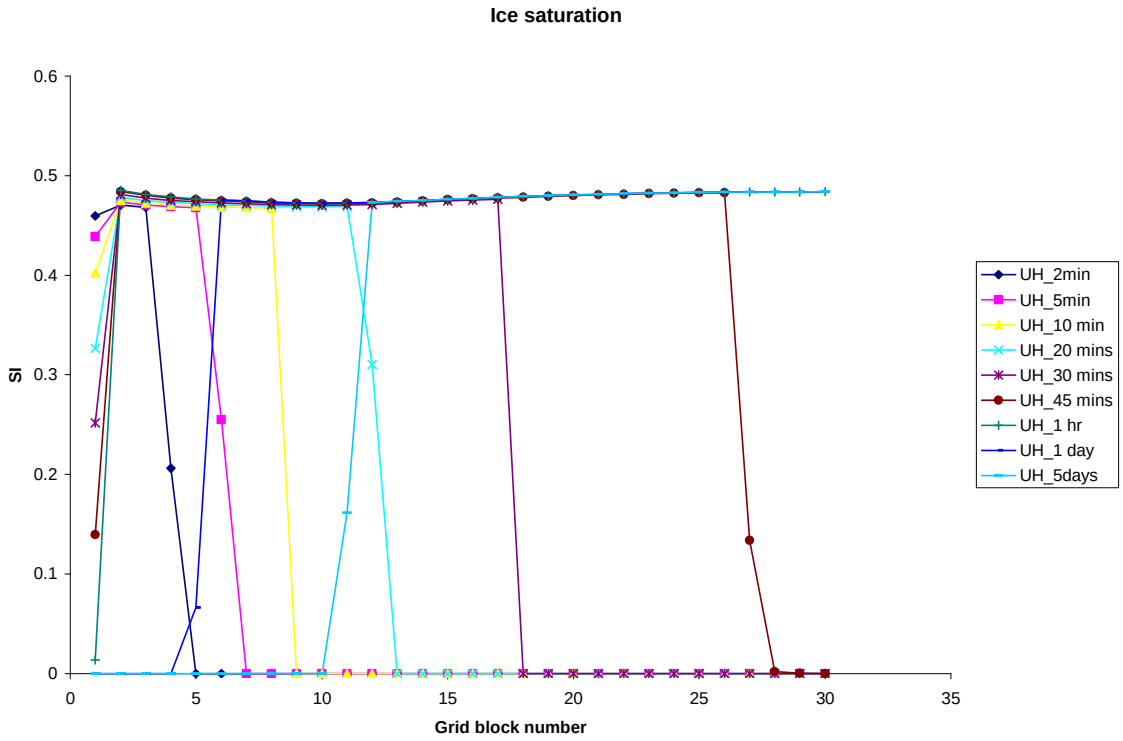

Fig. 12: Ice saturation evolution in problem 3.3

The results from our simulator for the problem 3.3 are plotted in Figs.8-12. Fig. 8 shows the temperature evolution. There is an initial temperature decrease because dissociation of hydrates uses up the latent heat. As the pressure decrease is very high, temperature decreases to the freezing point and ice formation starts, as shown in Fig 12. The temperature at x=0 is kept constant at T=6 °C so the heat flux from x=0 increases the temperature at the left grid blocks as the dissociation front moves away from the boundary. Ice melts as the temperature front moves. Fig. 10 shows the hydrate phase saturation. The gas pressure is not conveyed as quickly as in problem 3.2 (Fig. 11) because ice formation decreases the water permeability.

Problem 4

This is a one-dimensional problem in a radial domain for gas production using heat source at radius=0 and constant pressure / temperature condition at Rmax boundary. Initially only hydrate and aqueous phases are present in the domain. The results are recorded at the end of 2 days, 5 days, 10 days, 15 days, 20 days, 30 days, 45 days and 60 days. The results are plotted in Figs. 13-17 against r^2/t (m2/day), a key variable for a similarity solution of radial conduction. Most of the parameters (Sw, Sh, Sg, T) are functions of this similarity variable, r^2/t alone, where as the gas pressure is not. A dissociation front moves in radially. There is a high hydrate saturation zone just ahead of this dissociation front.

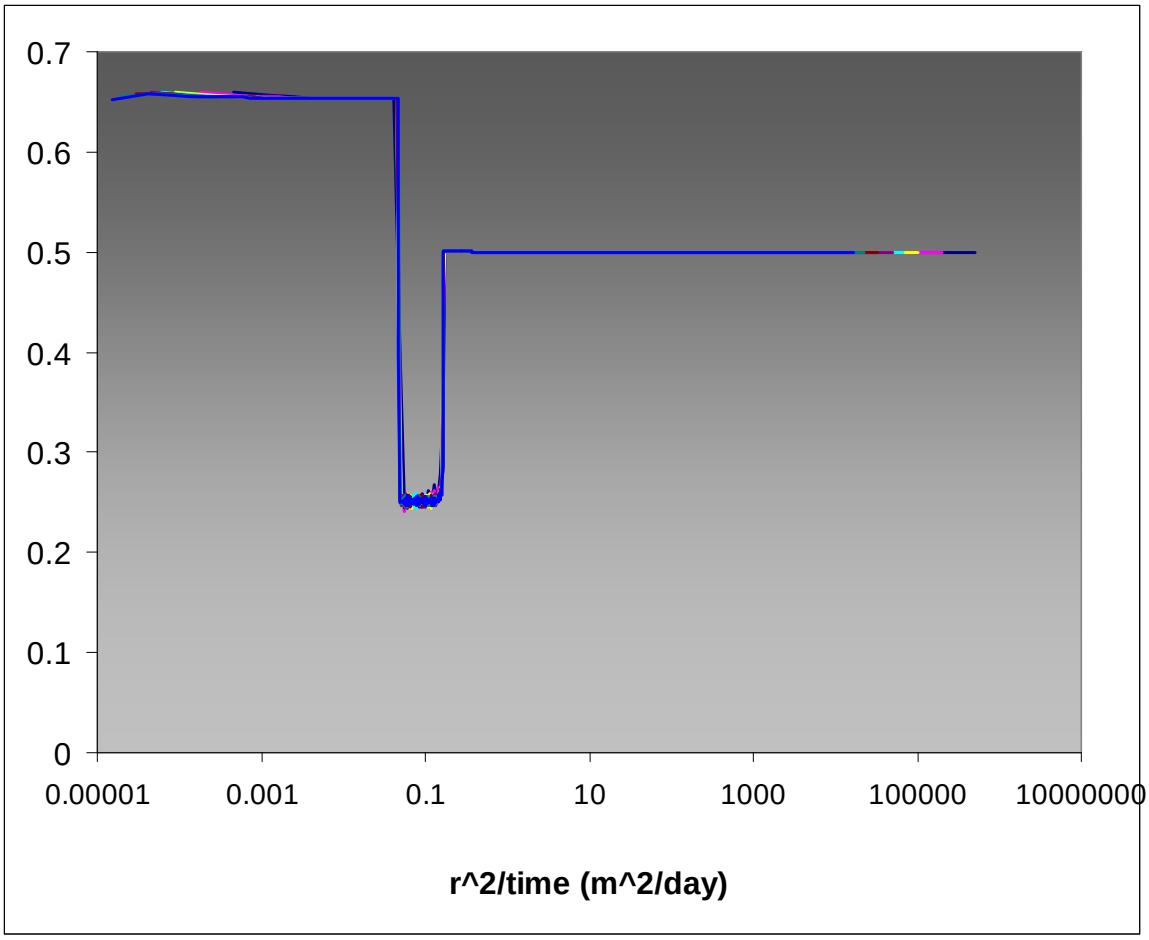

Fig 13: Aqueous Saturation

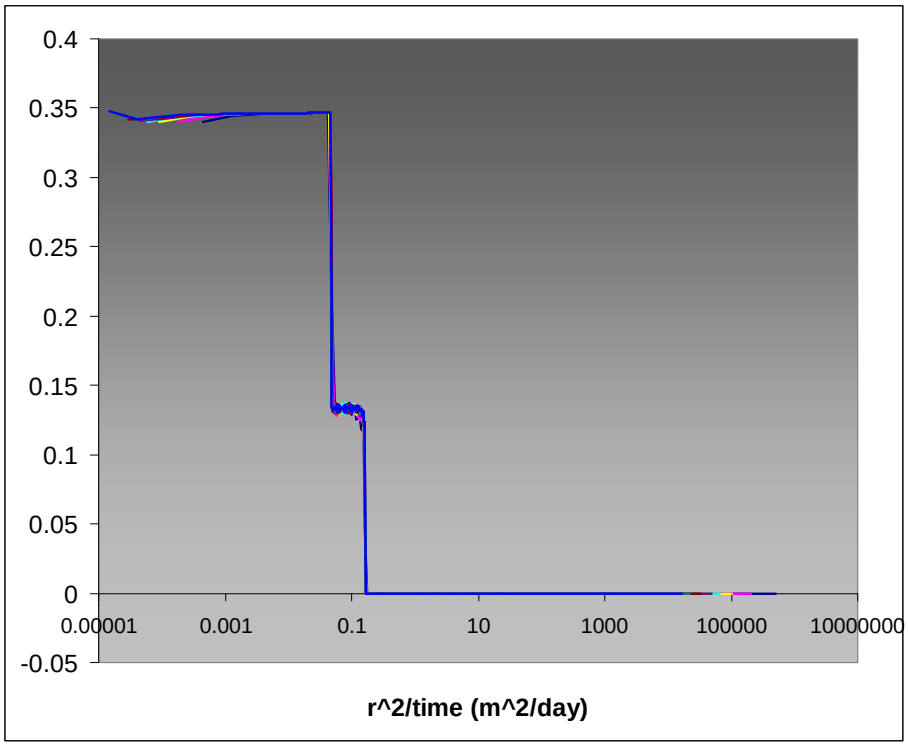

Fig 14: Gas saturation

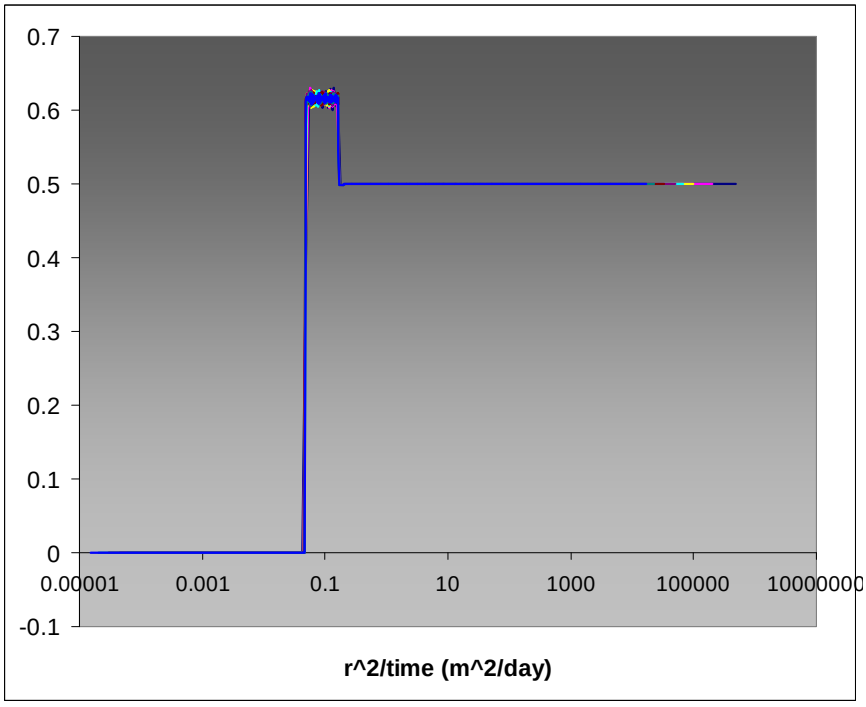

Fig 15: Hydrate saturation

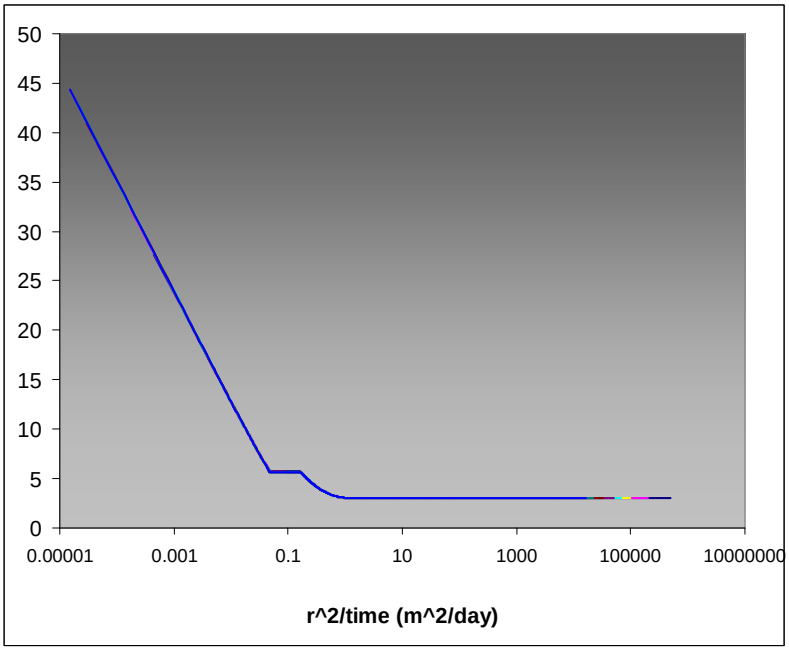

Fig 16: Temperature (ºC)

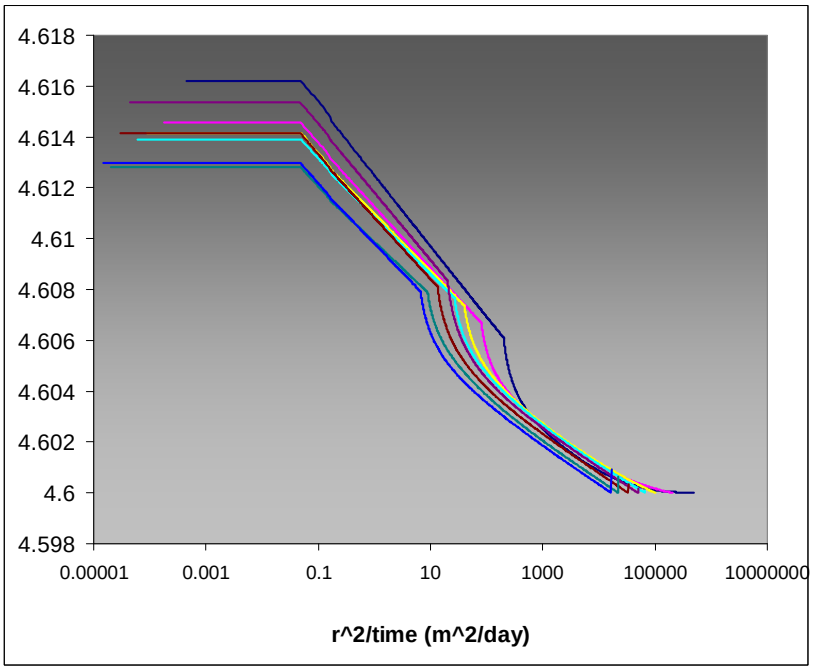

Fig 17: Gas pressure

Conclusions

These results compare very well with the results of the other simulators in the code comparison study. We have sent our results to Prof. Brian Anderson, the coordinator of the code comparison study.

Future Direction

We will complete all the problems of the code comparison study next month.

Task 8: Seafloor and Borehole Stability.

We have begun assessing the geomechanical properties of sediments that are hydrate free and those that have hydrate. Through laboratory experiments at Rice University, the permeability of sediments from Keathley Canyon (GOM JIP hydrate drilling province) has been documented. We have started comparing the laboratory permeability measurements with NMR logging data to assess how well NMR data can be used to evaluate permeability in fine-grained systems and to evaluate how hydrate saturation affects sediment permeability. We will continue characterizing flow properties as part of the sediment properties database.

Seafloor stability research is moving along two fronts: sediment properties and numerical modeling. We are compiling sediment strength properties from existing studies that provide estimates of shear strength at various confining stresses, consolidation states, and hydrate saturation. These data will be compiled for the sediment properties database. First-order numerical models of seafloor stability are being constructed so we can do sensitivity analyses on the conditions that drive failure. After these models have been benchmarked, we will evaluate the hydrate scenarios that can drive the systems to failure.

Research progress on sediment properties and seafloor stability was presented at the DOE-NETL Methane Hydrate Program Merit Review in Golden, CO. Based on the comments from the review, we will tailor our research approach to address the concerns and strengths noted by the review panel.

We have also been actively contributing to the GOM JIP field program as Dugan is a member of the site survey selection team. As part of the team, Dugan has been contributing to the characterization of the geologic setting of the proposed sites and the scientific objectives of each potential drill site. The site survey team will be presenting its recommendations to the JIP on 19 October 2009.

Task 9: Geophysical Imaging of Gas Hydrate and Free Gas Accumulations

Milestone 9.1: Preliminary processing and inversion of seismic data.

Perform conventional seismic reflection processing, velocity analysis, travel time tomography, and other analyses as deemed appropriate and necessary.

Milestone 9.2: Final 1-D elastic and 2-D acoustic waveform inversion.
Apply 1-D elastic and 2D acoustic inversions on data obtained from subtask 9.1 to derive determine high-resolution elastic and acoustic properties.

Milestone 9.3: Rock physics modeling.

Apply rock physics models to the developed seismic models to estimate hydrate saturation and lithology through application of well log data in conjunction with data from subtask 9.2. For this subtask we shall seek to collaborate with research being conducted under separately funded DOE-NETL projects (DE-FC26-05NT42663 with Stanford University, "Seismic-Scale Rock Physics of Methane Hydrate" and others as applicable).

COST PLAN / STATUS					
	Phase 1	Phase 2; Year 1 (June 2007-May 2008)			
Baseline Reporting Quarter		Q3/07	Q4/07	Q1/08	Q2/08
Baseline Cost Plan (SF-424A)					
Federal Share	$3,624	$80,003	$80,003	$80,003	$80,003
Non-Federal Share	$1,004	$28,653	$28,653	$28,653	$28,653
Total Planned	$4,628	$108,656	$108,656	$108,656	$108,656
Cumulative Baseline Cost	$4,628	$113,284	$221,940	$330,596	$439,252
Actual Incurred Cost					
Federal Share	$3,082	$56,282			
Non-Federal Share	$1,091	$18,616			
Total Planned	$4,173	$74,898			
Cumulative Costs	$4,173	$79,071			
Variance (plan-actual)					
Federal Share	$542	$23,721			
Non-Federal Share	$(87)	$10,037			
Total Variance	$455	$33,758			
Cumulative Variance	$455	$34,213			

Milestone Plan/Status

Task	Milestone: Status and Results	Date	Status
5. Carbon inputs and outputs to gas hydrate systems	5.1a Measure iodine in sediments We have measured iodine concentrations in pore waters from several gas hydrate systems. We hope to complete the analyses this month and write up intitial results over the next month.	12/07	1/08
	5.1b Constrain C_{org} inputs from iodine We will measure the content and isotopic composition of organic carbon and carbonate in sediment from cores of several gas hydrate systems. We have collected most of the samples, although plan to visit the ODP repository (College Station) in late spring or early summer to collect additional samples. Most analyses will be done this summer, although we anticipate examination of a small "trial batch" of samples from the Peru Margin in the next month.	10/08	
	5.2a Construct metal profiles in sediments We will measure metal contents in sediment from cores of several gas hydrate systems to constrain past hydrocarbon outputs via anaerobic oxidation of methane (AOM). Because initiation of project funding was slowed, we began some of this work last year with scientists from Japan using samples of opportunity from the Sea of Japan. This work was published in the fall (Snyder et al., 2007).	12/09	
	5.2b Modeling/integrating profiles We will use the metal and iodine profiles to constrain models for gas hydrate formation. We have discussed data and models but	12/10	

	have not begun this work so far.		
6. Numerical models for quantification of hydrate and free gas accumulations	6.1 Model development. The recipient shall develop finite difference models for the accumulation of gas hydrate and free gas in natural sediment sequences on geologically relevant time scales.	9/07	1/08
	6.2: Conditions for existence of gas hydrate The recipient shall summarize, quantitatively, the conditions for the absence, presence, and distribution of gas hydrates and free gas in 1-D systems by expressing the conditions in terms of dimensionless groups that combine thermodynamic, biological and lithologic transformation, and transport parameters.	3/07	done
	6.3 Compositional effect on BSR The recipient shall add to the numerical model, developed under this task, a chloride balance and multi-hydrocarbon capability specifically to investigate how hydrocarbon fractionation might affect Bottom Simulating Reflectors (BSRs).	7/07	12/08
	6.4: Amplitude Attenuation and chaotic zones due to hydrate distribution The recipient shall simulate preferential formation of gas hydrate in coarse-grained, porous sediment in 2-D by linking fluid flux to the permeability distribution.	3/09	
	6.5: Processes leading to overpressure The recipient shall quantify, by simulation and summarize by combination of responsible dimensionless groups, the conditions leading to overpressure to the point of sediment failure.	3/08	
	6.6 Concentrated hydrate and free gas The recipient shall, using 2-D and 3-D models, simulate lateral migration and concentration of gas hydrate and free gas in structural and stratigraphic traps.	3/08	

	6.7 Focused free gas, heat and salinity The recipient shall quantify, using 2-D and 3-D model simulations and comparisons to available observations, the factors controlling the process of localized upward migration of free gas along faults and lateral transfer to dipping strata that can lead to chaotic zones and possible accumulations of concentrated hydrate.	9/09	
	6.8 Sulfate profile as indicator of methane flux The recipient shall compute, for systems where data on the sulfate profile is available, the oxidation of methane by sulfate and shall indicate the perceived level of effect on gas hydrate accumulation and the data's value as an indicator of methane flux.	7/07	12/07
	6.9 Application of models to interpretation of case studies. The models developed in Task 6 will be applied to case studies in the interpretation of each of the other tasks.	6/10	6/10
7. Analysis of production strategy	7.1a Pore scale model development and Hydrate code comparison For this milestone, we will develop pore-scale models of hydrate accumulation by simulation. Our hydrate code will be used to solve a set of problems formulated by the Code Comparison Study group. Our results will be compared with those of other hydrate codes. Should be changed to: 6/08 Reason: The starting date was moved to 6/07 Status: Code comparison study is 80% complete.	1/08	6/08
	7.1b Petrophysical and thermophysical properties of hydrate sediments from pore-scale model For this milestone, we will assume the	1/09	6/09

	pore-scale models of hydrate accumulation developed in the last milestone and estimate transport properties as a function of hydrate and gas saturations. Should be changed to: 6/09 Reason: The starting date was moved to 6/07 Status: Have not started		
	7.2a Modeling of several production strategies to recover gas from marine hydrates Several production strategies would be modelled using the transport property correlations developed in the previous milestone. Optimal strategies will be identified. Should be changed to: 6/10 Reason: The starting date was moved to 6/07 Status: Have not started	1/10	6/10
	7.2b Effect of marine reservoir heterogeneities on production of methane Reservoir heterogeneity anticipated in marine environments (known or determined through other tasks) would be incorporated. Appropriate hydrate distributions, either constrained from experimental data or mechanistic simulations (Task 5) would be used. Sensitivity of gas production to the heterogeneities would be calculated. Should be changed to: 6/11 Reason: The starting date was moved to 6/07 Status: Have not started	12/10	6/10
8. Seafloor and borehole stability	8.1a Collection of data Status: 05/08 (large shift according to anticipated start date and dispersement of funds to Rice) To achieve this milestone, we will perform a literature and database search of existing geomechanical properties of sediments with hydrate and sediments without hydrate from hydrate	10/07	05/08

	settings. This will include laboratory experiments, field data, published results, and unpublished data.		
	8.1c Complete database Status: 1/09 (some shift due to delay of data collection) We will organize the data from task 8.1a into a format that can be easily searched and used by any researchers trying to understand mechanical behavior of hydrate-bearing sediment. We will also identify key gaps in the database for focusing future hydrate research endeavors.	10/08	01/09
	8.2a Link database with models Status: 8/08 From the database we will assess how hydrate saturation affects different geomechanical properties. These relationships can then be input into models of basin development or production.	3/08	8/08
	8.2b Add sediment stability to models Status: 10/08 Standard stability calculations will be coupled with basin scale and production models. The strength characteristics that influence stability will be imported from the relations developed in 7.2a.	10/08	
	8.2c Conditions for (in)stability	9/09	
9 Geophysical imaging of hydrate and free gas	9.1 Preliminary processing and inversion of seismic data. Perform conventional seismic reflection processing, velocity analysis, travel time tomography, and other analyses as deemed appropriate and necessary.	8/08	
	9.2: Final 1-D elastic and 2-D acoustic waveform inversion. Apply 1-D elastic and 2D acoustic inversions on data obtained from subtask 9.1 to derive determine high-resolution	8/09	

	elastic and acoustic properties.		
	9.3: Rock physics modeling. Apply rock physics models to the developed seismic models to estimate hydrate saturation and lithology through application of well log data in conjunction with data from subtask 9.2. For this subtask we shall seek to collaborate with research being conducted under separately funded DOE-NETL projects (DE-FC26-05NT42663 with Stanford University, "Seismic-Scale Rock Physics of Methane Hydrate" and others as applicable).	8/10	

UPCOMING PRESENTATIONS RELATED TO NETL PROJECTS

For the quarter ending December 31, 2007

Presentation

Title
Correlations and Proxies for Methane Hydrate Accumulation in Marine Sediments
Date
November 26, 2008
Location
University of Texas at Austin

Speaker (check one)

Principal Investigator (Name and E-mail Address)

x Project Manager (Name and E-mail Address)
George Hirasaki, gjh@rice.edu
Other (Name and E-mail address)

Sponsor/Organizer of Presentation Venue (SPE, AAPG, IADC, etc.)

UT Petroleum Engineering Department

Related NETL Project

Project Title
Detection and Production of Methane Hydrate
Project Number
DE-FC26-06NT42960

Presentation Abstract

It is estimated that there is more hydrocarbon stored as methane hydrate in marine sediments and permafrost that all of the known coal, oil and gas resources. The presence of methane hydrate is usually recognized by “bottom simulating reflections” in seismic records due to the contrast in the acoustic impedance at the base of the hydrate stability zone. However, most of the methane hydrate is distributed at low concentrations that may not be economic for production. Techniques are needed to quantify the amount of methane hydrates that may be present in an accumulation.

Analysis has been completed in 1-D to quantify the methane hydrate saturation when the source for methane is either biogenic or dissolved in water from deeper sources. The steady-state average hydrate saturation has been correlated as a function of a few dimensionless groups.

The depth of the sulfate-methane transition zone has been used as a proxy for the methane flux from deeper sources. When the only methane source is from deeper sources, the 1-D, steady-state profile of the hydrate saturation can be determined from the knowledge of the depth of the sulfate-methane transition zone.

These correlations and analytical solutions are compared with observations from several sites.

UPCOMING PRESENTATIONS RELATED TO NETL PROJECTS
For the quarter ending December 31, 2007

Presentation

Title
Effects of Seafloor Temperature on the Distribution of Methane Hydrate
Date
10-14 December 2007
Location
San Francisco

Speaker
(check one)

Principal Investigator (Name and E-mail Address)

Project Manager (Name and E-mail Address)

x Other (Name and E-mail address)
Guangsheng Gu, gg2@rice.edu

Sponsor/Organizer of Presentation Venue (SPE, AAPG, IADC, etc.)

AGU
Website Address
http://www.agu.org/
Telephone Number

Related NETL Project

Project Title

Project Number

Presentation Abstract

Deep ocean temperatures were 10-15 deg C warmer than present-day during the Early Cretaceous and Early Paleogene. Such temperatures would impact the distribution of gas hydrate in marine sediment. Clearly, the vertical extent of the Gas Hydrate Stability Zone (GHSZ) and the overall volume of sediment hosting gas hydrates at shallow water depths would be smaller than at present-day. Several authors have taken this to mean that overall amounts of gas hydrate and methane in marine sediments were much smaller in ancient warm oceans. However, this inference may be incorrect. In any case, it has not been appropriately evaluated. We have developed a one-dimensional numerical model that describes the formation and distribution of methane hydrate in marine sediment on geological time scales. Here we modify this model to examine the effect of changing seafloor temperature from 3 to 18 deg C in cases where microbial activity supplies most of the methane. Predictably, the temperature increase shifts the methane solubility curve in marine sediment and decreases the depth of the GHSZ. Less obvious but more important are temperature effects on the flux of seafloor organic carbon and the rate of methanogenesis. In some cases, increased seafloor temperature results in decreased amounts of methane hydrate. However, in other simulations, when seafloor organic fluxes and biogenic reaction rates increase significantly, amounts of methane hydrate can be higher than modeled for the present-day. It is possible that, during times of warm oceans, greater amounts of organic carbon enter the seafloor, microbes make methane from this carbon at much faster rates, and gas hydrate quantities exceed those at present-day. These somewhat counter-intuitive

National Energy Technology Laboratory

626 Cochrans Mill Road
P.O. Box 10940
Pittsburgh, PA 15236-0940

3610 Collins Ferry Road
P.O. Box 880
Morgantown, WV 26507-0880

One West Third Street, Suite 1400
Tulsa, OK 74103-3519

1450 Queen Avenue SW
Albany, OR 97321-2198

2175 University Ave. South
Suite 201
Fairbanks, AK 99709

Visit the NETL website at:
www.netl.doe.gov

Customer Service:
1-800-553-7681